

Fabrication and characterization of periodically patterned silica fiber structures for enhanced second-order nonlinearity

Chalongrat Daengngam,^{1,4} Ishac Kandas,^{2,3} Islam Ashry,^{2,3} Anbo Wang,² James R. Heflin,¹ and Yong Xu^{2,*}

¹Department of Physics, Virginia Tech, Blacksburg, Virginia 24061, USA

²The Bradley Department of Electrical and Computer Engineering, Virginia Tech, Blacksburg, Virginia 24061, USA

³Department of Engineering Mathematics and Physics, Faculty of Engineering, Alexandria University, Alexandria 21526, Egypt

⁴Department of Physics, Faculty of Science, Prince of Songkla University, Hatyai, Songkhla 90110, Thailand
[*yong@vt.edu](mailto:yong@vt.edu)

Abstract: We develop and characterize a UV ablation technique that can be used to pattern soft materials such as polymers and nonlinear molecules self-assembled over silica microstructures. Using this method, we fabricate a spatially periodic coating of nonlinear film over a thin silica fiber taper for second harmonic generation (SHG). Experimentally, we find that the second harmonic signal produced by the taper with periodic nonlinear coating is 15 times stronger than the same taper with uniform nonlinear coating, which suggests that quasi-phase-matching is at least partially achieved in the patterned nonlinear silica taper. The same technique can also be used to spatially pattern other types of functional nanomaterials over silica microstructures with curved surfaces, as demonstrated by deposition of gold nanoparticles in patterned structures.

©2015 Optical Society of America

OCIS codes: (060.3510) Lasers, fiber; (190.0190) Nonlinear optics; (310.0310) Thin films.

References and links

1. M. L. Gorodetsky, A. A. Savchenkov, and V. S. Ilchenko, "Ultimate Q of optical microsphere resonators," *Opt. Lett.* **21**(7), 453–455 (1996).
2. B. P. Antonyuk, N. N. Novikova, N. V. Didenko, and O. A. Aktsipetrov, "All optical poling and second harmonic generation in glasses: theory and experiment," *Phys. Lett. A* **287**(1-2), 161–168 (2001).
3. M. K. Balakirev, V. A. Smirnov, and L. I. Vostrikova, "Photorefractive effect on all optical polling of glass," *J. Opt. A, Pure Appl. Opt.* **5**(6), S437–S443 (2003).
4. R. A. Myers, N. Mukherjee, and S. R. J. Brueck, "Large second-order nonlinearity in poled fused silica," *Opt. Lett.* **16**(22), 1732–1734 (1991).
5. A. Canagasabey, C. Corbari, A. V. Gladyshev, F. Liegeois, S. Guillemet, Y. Hernandez, M. V. Yashkov, A. Kosolapov, E. M. Dianov, M. Ibsen, and P. G. Kazansky, "High-average-power second-harmonic generation from periodically poled silica fibers," *Opt. Lett.* **34**(16), 2483–2485 (2009).
6. T. Fujiwara, M. Takahashi, and A. J. Ikushima, "Second-harmonic generation in germanosilicate glass poled with ArF laser irradiation," *Appl. Phys. Lett.* **71**(8), 1032–1034 (1997).
7. C. Corbari, P. G. Kazansky, S. A. Slattery, and N. Nikogosyan, "Ultraviolet poling of pure fused silica by high-intensity femtosecond radiation," *Appl. Phys. Lett.* **86**, 071106 (2005).
8. A. Okada, K. Ishii, K. Mito, and K. Sasaki, "Phase-matched second-harmonic generation in novel corona poled glass waveguides," *Appl. Phys. Lett.* **60**(23), 2853–2855 (1992).
9. S. Horinouchi, H. Imai, G. J. Zhang, K. Mito, and K. Sasaki, "Optical quadratic nonlinearity in multilayer corona-poled glass films," *Appl. Phys. Lett.* **68**(25), 3552–3554 (1996).
10. J. R. Heflin, M. T. Guzy, P. J. Neyman, K. J. Gaskins, C. Brands, Z. Wang, H. W. Gibson, R. M. Davis, and K. E. Van Cott, "Efficient, thermally stable, second order nonlinear optical response in organic hybrid covalent/ionic self-assembled films," *Langmuir* **22**(13), 5723–5727 (2006).
11. Y. Xu, A. Wang, J. R. Heflin, and Z. Liu, "Proposal and analysis of a silica fiber with large and thermodynamically stable second order nonlinearity," *Appl. Phys. Lett.* **90**(21), 211110 (2007).

12. Y. Xu, M. Han, A. Wang, Z. Liu, and J. R. Heflin, "Second order parametric processes in nonlinear silica microspheres," *Phys. Rev. Lett.* **100**(16), 163905 (2008).
13. C. Daengngam, M. Hofmann, Z. Liu, A. Wang, J. R. Heflin, and Y. Xu, "Demonstration of a cylindrically symmetric second-order nonlinear fiber with self-assembled organic surface layers," *Opt. Express* **19**(11), 10326–10335 (2011).
14. V. Grubsky and J. Feinberg, "Phase-matched third-harmonic UV generation using low-order modes in a glass micro-fiber," *Opt. Commun.* **274**(2), 447–450 (2007).
15. U. Wiedemann, K. Karapetyan, C. Dan, D. Pritzkau, W. Alt, S. Irsen, and D. Meschede, "Measurement of submicrometre diameters of tapered optical fibres using harmonic generation," *Opt. Express* **18**(8), 7693–7704 (2010).
16. J. Tien, A. Terfort, and G. M. Whitesides, "Microfabrication through electrostatic self-assembly," *Langmuir* **13**(20), 5349–5355 (1997).
17. Y. H. Kim, J. Park, P. J. Yoo, and P. T. Hammond, "Selective assembly of colloidal particles on a nanostructured template coated with polyelectrolyte multilayers," *Adv. Mater.* **19**(24), 4426–4430 (2007).
18. S. V. Stoianov, C. Daengngam, M. Borhani, Y. Zhang, J. R. Morris, and H. D. Robinson, "Amine-rich polyelectrolyte multilayers for patterned surface fixation of nanostructures," *ACS Appl. Mater. Interfaces* **4**(5), 2348–2357 (2012).
19. H. Nakayama, O. Sugihara, and N. Okamoto, "Nonlinear optical waveguide fabrication by direct electron-beam irradiation and thermal development using a high T_g polymer," *Appl. Phys. Lett.* **71**(14), 1924–1926 (1997).
20. A. Rastogi, M. Y. Paik, M. Tanaka, and C. K. Ober, "Direct patterning of intrinsically electron beam sensitive polymer brushes," *ACS Nano* **4**(2), 771–780 (2010).
21. C. Aubry, T. Trigaud, J. P. Moliton, and D. Chiron, "Polymer gratings achieved by focused ion beam," *Synth. Met.* **127**(1-3), 307–311 (2002).
22. M.-W. Moon, J. H. Han, A. Vaziri, E. K. Her, K. H. Oh, K.-R. Lee, and J. W. Hutchinson, "Nanoscale ripples on polymers created by a focused ion beam," *Nanotechnology* **20**(11), 115301 (2009).
23. M. Nakanishi, O. Sugihara, N. Okamoto, and K. Hirota, "Ultraviolet photobleaching process of azo dye doped polymer and silica films for fabrication of nonlinear optical waveguides," *Appl. Opt.* **37**(6), 1068–1073 (1998).
24. O. Watanabe, M. Tsuchimori, and A. Okada, "Two-step refractive index changes by photoisomerization and photobleaching processes in the films of non-linear optical polyurethanes and a urethane-urea copolymer," *J. Mater. Chem.* **6**(9), 1487–1492 (1996).
25. T. Hattori, T. Shibata, S. Onodera, and T. Kaino, "Fabrication of refractive index grating into azo-dye-containing polymer films by irreversible photoinduced bleaching," *J. Appl. Phys.* **87**(7), 3240–3244 (2000).
26. H. Masuhara, H. Hiraoka, and E. E. Martinero, "Non-linear photochemistry of polymer films: laser ablation of poly (n-vinylcarbazole)," *Chem. Phys. Lett.* **135**(1-2), 103–108 (1987).
27. B. Brochers, J. Bekesi, P. Simon, and J. Ihlemann, "Submicron surface patterning by laser ablation with short UV pulses using a proximity phase mask setup," *J. Appl. Phys.* **107**(6), 063106 (2010).
28. J. C. Chon and P. B. Comita, "Laser ablation of nonlinear-optical polymers to define low-loss optical channel waveguides," *Opt. Lett.* **19**(22), 1840–1842 (1994).
29. N. Bityurin, B. S. Luk'yanchuk, M. H. Hong, and T. C. Chong, "Models for laser ablation of polymers," *Chem. Rev.* **103**(2), 519–552 (2003).
30. M. Park, B. H. Chon, H. S. Kim, S. C. Jeoung, D. Kim, J.-I. Lee, H. Y. Chu, and H. Rae Kim, "Ultrafast laser ablation of indium tin oxide thin films for organic light-emitting diode application," *Opt. Lasers Eng.* **44**(2), 138–146 (2006).
31. I. Kandas, B. Zhang, C. Daengngam, I. Ashry, C.-Y. Jao, B. Peng, S. K. Ozdemir, H. D. Robinson, J. R. Heflin, L. Yang, and Y. Xu, "High quality factor silica microspheres functionalized with self-assembled nanomaterials," *Opt. Express* **21**(18), 20601–20610 (2013).
32. T.-C. Poon and T. Kim, *Engineering Optics with Matlab* (Word Scientific Publishing, 2008).
33. I. Ashry, I. Kandas, X. Wei, J. A. Calderone, B. Zhang, H. D. Robinson, J. R. Heflin, W. L. Santos, and Y. Xu, "Impact of lithography on the fluorescence dynamics of self-assembled fluorophores," *Opt. Express* **22**(11), 12935–12943 (2014).
34. I. H. Malitson, "Interspecimen comparison of the refractive index of fused silica," *J. Opt. Soc. Am.* **55**(10), 1205–1209 (1965).
35. A. Camara, O. Tarasenko, and W. Margulis, "Study of thermally poled fibers with a two-dimensional model," *Opt. Express* **22**(15), 17700–17715 (2014).
36. S. M. Tseng and C. L. Chen, "Side-polished fibers," *Appl. Opt.* **31**(18), 3438–3447 (1992).
37. G. Wu and Z. Wang, "Propagation characteristics of multi-coating D-shaped optical fibres," *J. Opt. A, Pure Appl. Opt.* **8**(5), 450–453 (2006).
38. W. Jin, H. L. Ho, Y. C. Cao, J. Ju, and L. F. Qi, "Gas detection with micro- and nano-engineered optical fibers," *Opt. Fiber Technol.* **19**(6), 741–759 (2013).
39. S. H. Behrens and D. G. Grier, "The charge of glass and silica surfaces," *J. Chem. Phys.* **115**(14), 6716–6721 (2001).

1. Introduction

Silica glass, with extremely low material absorption, is one of the most important materials for photonics and optoelectronics. Silica fibers, operated in the near infrared, are essential for long haul optical communications. By melting silica glass, one can also produce extremely smooth air-silica interfaces with minimal scattering loss. Taking advantage of this feature, silica glass has been used in the fabrication of high quality (Q) factor optical resonators [1]. However, due to the lack of second-order nonlinearity, silica glass is unsuitable for certain applications that require strong light-light interaction, such as second-order parametric amplification and down conversion. Therefore, to further extend the reach of fiber optic technology, it is desirable to introduce functionalities such as second-order nonlinearity into silica based structures.

In order to incorporate second-order nonlinearity into silica-based fiber structures, most existing methods rely on various poling techniques such as optical poling [2,3], electrical poling [4,5], UV poling [6,7], and corona poling [8,9]. A major drawback of these methods is that poling-induced second-order nonlinearity is thermodynamically unstable and tends to decay over time. Recently, we demonstrated a thermodynamically stable second-order nonlinear fiber by coating a silica taper with hybrid covalent/ionic self-assembled multilayers of poly(allylamine hydrochloride) (PAH) and radially aligned nonlinear molecules Procion Brown MX-GRN (PB) [10–13]. However, in our previous report, since the fundamental pump and the second harmonic signal are not phase matched, the efficiency of second harmonic generation (SHG) by the nonlinear taper is very low. Similarly, relying on the surface nonlinearity at the air-silica interface, other researchers have also demonstrated SHG using bare silica fiber tapers [14,15]. Again, due to the inability to achieve phase matching, the SHG efficiency of bare silica fiber tapers is typically of the order of 10^{-8} with 400 W peak pump power [13]. In this paper, we aim to overcome this challenge and establish a methodology for quasi-phase-matching (QPM), where we utilize laser ablation to periodically pattern a silica fiber taper functionalized with nonlinear molecules, as shown in Fig. 1. With appropriate periodicity, second harmonic signals produced by the nonlinear coating at different taper sections can be coherently added together in phase, thus significantly enhancing the efficiency of SHG. Experimentally, we find that SHG signals produced by a periodically patterned nonlinear taper significantly exceed those generated by a uniformly coated nonlinear taper, thus confirming the feasibility of QPM.

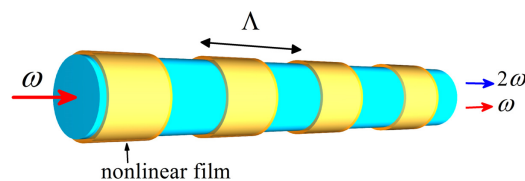


Fig. 1. Optical fiber taper with periodically patterned nonlinear surface layers for SHG.

To the best of our knowledge, no literature has previously reported how to realize QPM for silica-based fiber taper structures. Additionally, the laser ablation technique described here can also be used to selectively pattern other types of silica microstructures (e.g., microspheres and micro-toroids) with nanomaterials such as second-order nonlinear molecules as well as various nanoparticles (NPs) and biomolecules. As a proof of concept demonstration of patterned NP deposition, in this paper, we show that it is possible to attach gold (Au) NPs onto a silica fiber taper in a spatially selective manner. The key difference between our approach and other existing methods [16–18] is that we utilize laser ablation to generate the desired surface charge distribution for spatially selective patterning. Compared with other approaches, the laser ablation technique can have significant advantages, such as large patterning area, fast patterning time, no need for chemical etching or complicated

lithography, and compatibility with a myriad of device configurations, substrate materials, and functional nanomaterials.

2. Laser ablation characterization

In existing literature, several techniques have been developed for micro- and nano-scale patterning of soft materials such as polymers. For example, direct writing on polymer films using an electron beam [19,20] or a focused ion beam (FIB) [21,22] can produce well-defined patterns with high resolution. The process of e-beam or FIB lithography, however, is slow, expensive, and unsuitable for large scale structures such as a fiber taper with periodic $\chi^{(2)}$ grating for QPM, which may contain hundreds of stripes and exceed several millimeters in total length. Alternatively, it is also possible to use deep UV irradiation to photobleach azo-dyes such as PB to form spatially periodic $\chi^{(2)}$ gratings [23–25]. However, the photobleaching process can sometimes be quite slow, and perhaps more importantly, is unsuitable for patterning other types of functional nanomaterials.

UV laser ablation has been used to remove soft materials such as polymers in a controllable manner and with minimal thermal damage to the underlying structures. Upon irradiation of a high-intensity laser beam, the soft materials absorb the high-energy photons and undergo bond breaking. If the beam energy is high enough, the material will be volatilized quickly and the mass will be ejected into the air, leaving a clean substrate surface with almost no residue. Experimentally, it has been found that even a single pulse of a UV laser is capable of removing several-micron-thick polymer films solely by the photochemical process [26,27]. Due to the short time scale required for UV ablation, thermal damage tends to be minimal or virtually non-existent.

This brief survey suggests that UV ablation is potentially ideal for patterning self-assembled polymer films. However, to the best of our knowledge, only one paper [28] has ever utilized laser ablation to fabricate channel waveguides containing nonlinear polymers. However, the nonlinear optical properties of the channel waveguides were not characterized. Additionally, UV ablation has never been attempted in the context of self-assembled soft materials exhibiting second-order nonlinearity.

2.1 Ablation patterning of self-assembled PAH/PB films on planar substrates

Prior to patterning a cylindrical fiber taper, we first investigate the laser ablation of nonlinear films self-assembled over a planar glass substrate. Our purposes are two-fold: to determine the intensity dependence of laser ablation, and to ensure that the film retains its nonlinearity after ablation. In UV ablation, the most important parameter is the energy threshold required to remove the film. This can be determined by measuring the depth of a crater-like profile on the film surface caused by exposure to a single laser pulse with different fluence. In actual experiments, we begin sample preparation by depositing a thick layer of PAH/PB film (600 bilayers, ~350 nm in thickness) on a flat glass slide. To control crater size, we place a metallic pinhole with 20 μm diameter directly on top of the sample surface as a mask. The sample, covered everywhere except at the pinhole, is exposed to a single pulse of collimated excimer laser beam (248 nm, MPB Technologies). The beam fluence can be adjusted using a UV-grade lens set that expands or compresses the beam. The laser pulse duration is 10 ns, unfocused beam size is ~1 cm^2 , the pulse repetition rate ranges from 0.5 to 10 Hz, and its maximum output fluence is 1500 mJ/cm^2 . Even a single laser pulse can produce a detectable crater. Its depth profile is measured using a profilometer (Veeco Dektak 150).

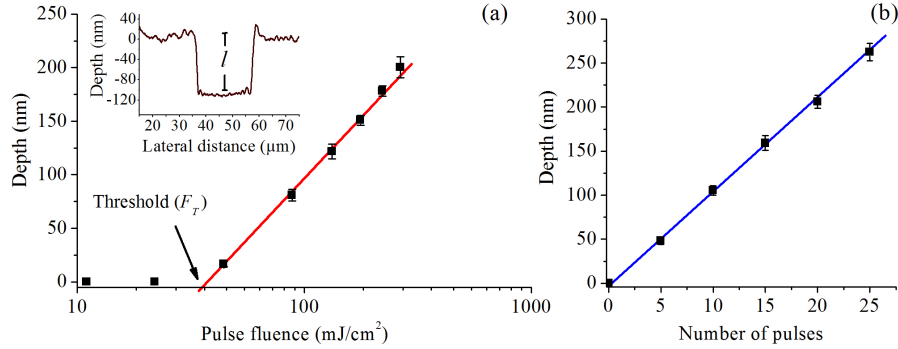


Fig. 2. (a) The depth of the crater caused by single-pulse ablation versus pulse fluence. The inset shows a representative crater profile obtained using a surface profilometer. (b) The crater depth as a function of the number of pulses used in laser ablation, with pulse fluence fixed at $F = 45 \text{ mJ/cm}^2$.

Figure 2(a) shows the dependence of crater depth on single pulse fluence. Clearly, below a certain threshold (F_T), the UV laser has little impact on the polymer. However, once the threshold fluence is reached, a stronger pulse generates a deeper crater. This behavior is a characteristic feature of laser ablation, and can be empirically described by [29]:

$$l = \frac{1}{\alpha} \ln \left(\frac{F}{F_T} \right), \quad (1)$$

where l is the ablation depth per pulse, α is the absorption coefficient of the film at the laser wavelength, F is the laser fluence used, and F_T is the fluence threshold of the material. From the linear fitting in Fig. 2(a), the value of F_T for the PAH/PB film is $\sim 40 \text{ mJ/cm}^2$. This value is much lower than the fluence threshold of glass, typically in the range of $1200\text{--}1600 \text{ mJ/cm}^2$ [30]. Therefore, this result indicates that UV ablation can be used to pattern the self-assembled PAH/PB film without damaging the underlying silica substrate.

We also investigate the relationship between ablation depth and the number of laser pulses for fixed pulse fluence. Our results in Fig. 2(b) suggest that the ablation depth increases linearly as a function of the pulse number. The pulse fluence here is chosen to be 45 mJ/cm^2 , which is slightly above the threshold. Even at this low beam fluence, the ablation rate can be as fast as ~ 10 bilayers per pulse. Under the maximum pulse repetition rate of 10 Hz , patterning a 50 -bilayer PAH/PB film can be finished within a second. In practice, however, we usually ablate the samples for a longer time (e.g. a few minutes) to ensure that the laser pulses completely remove all possible residual mass, *without* damaging the glass substrate.

2.2 SHG from patterned PAH/PB on planar glass

The next step in characterization is to ensure that the patterned PAH/PB film retains its second order nonlinear susceptibility $\chi^{(2)}$. For the ease of experiments, the characterization of $\chi^{(2)}$ is again carried out using a planar glass slide with a patterned PAH/PB film, as shown in Fig. 3(a). The designed pattern contains three stripes of 150 -bilayer film with stripe width of $500 \mu\text{m}$ and equal distance in between. A pump beam generated by an OPO (pulse duration $\sim 10 \text{ ns}$, peak power $P_\omega \sim 50 \text{ W}$) is launched in free space and focused onto the sample ($\sim 30 \mu\text{m}$ in focal beam diameter). The sample is mounted to a motorized stage, which allows us to scan the focused pump beam across the patterned PAH/PB stripes in $50 \mu\text{m}$ step size. At each scanning position the SHG signal is collected by a PMT, as shown in Fig. 3(b). A similar setup is used to measure nonlinear taper SHG, and is described in more detail below.

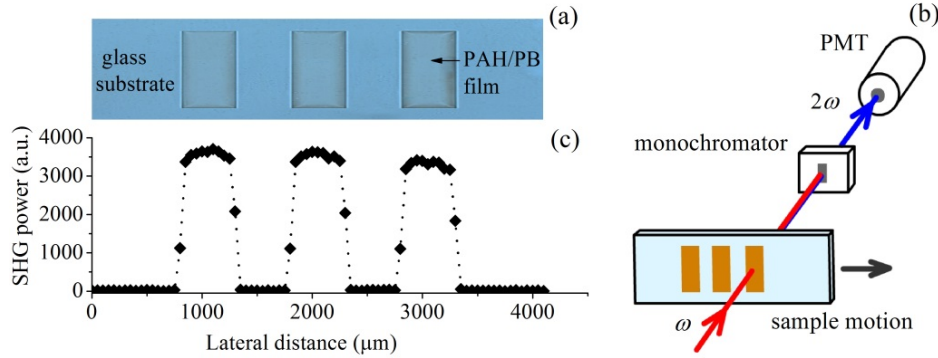


Fig. 3. (a) A phase-contrast optical microscope image of ablated PAH/PB film on a planar glass substrate. (b) A schematic of the experimental setup for measuring SHG from the patterned PAH/PB film, where the sample is scanned across a focused pump beam. (c) SHG power versus sample position.

The measured SHG signal intensity, shown in Fig. 3(c), clearly confirms that the PAH/PB film stripes that are not exposed to UV ablation retain their second-order nonlinearity, which is essential for achieving QPM. The lower SHG intensity measured at the edge of the film stripes is likely due to the finite pump beam size.

3. Fabrication and characterization of periodically patterned nonlinear fiber tapers

3.1 Taper fabrication and ablation

The fabrication of a periodically patterned nonlinear fiber taper begins with taper pulling, similar to our previous work [13]. In order to enhance optical coupling efficiency, we again use a standard multimode fiber (50 μm core diameter) for taper fabrication. The optical image of the whole fiber taper and the corresponding radius profile are illustrated in Fig. 4. Afterwards, the fiber taper is coated with bilayers of PAH and PB using the technique described in [13]. The PAH/PB film possesses stable and well-defined dipole orientation, thus imparting strong and thermodynamically stable $\chi^{(2)}$ onto the surface of the silica taper. The properties of these PAH/PB films have been extensively characterized in our prior work [10–13,31].

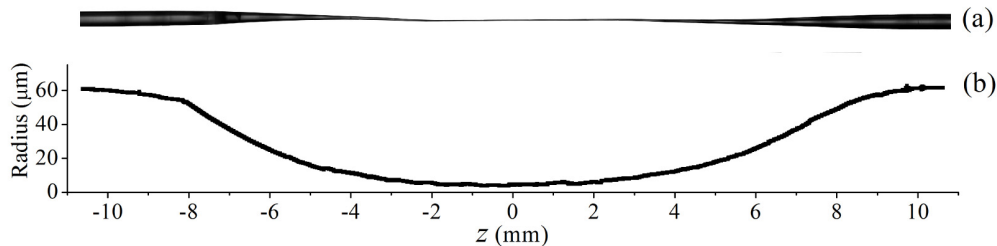


Fig. 4. (a) A microscope image of the whole taper structure, including both the waist and the transition regions. (b) The radial profile of the fiber taper extracted from the microscope image in (a).

UV laser ablation is carried out using a custom mask (Creative MicroSystems) that contains an array of 25 μm wide slits. Its spatial periodicity Λ is 50 μm , which is suitable for QPM in the nonlinear taper. (Refer to the calculation in section 5.1.) The mask contains an 800-nm-thick aluminum layer on a UV-transparent fused silica substrate. To withstand the beam intensity required for laser ablation, the metal coating of the ablation mask is much thicker than photomasks for standard UV lithography. The laser ablation process for the

nonlinear taper is similar to the patterning of the planar substrate except for one major difference: It is extremely difficult to place the ablation mask in direct contact with the taper surface, due to its curved geometry. Therefore, to keep fabrication simple, we place the mask directly on top of the entire fiber, as illustrated in Fig. 5(a). Consequently, there is always a 55-70 μm gap between the mask and the taper surface. As a result, we need to account for the effect of optical diffraction in analyzing the ablation process.

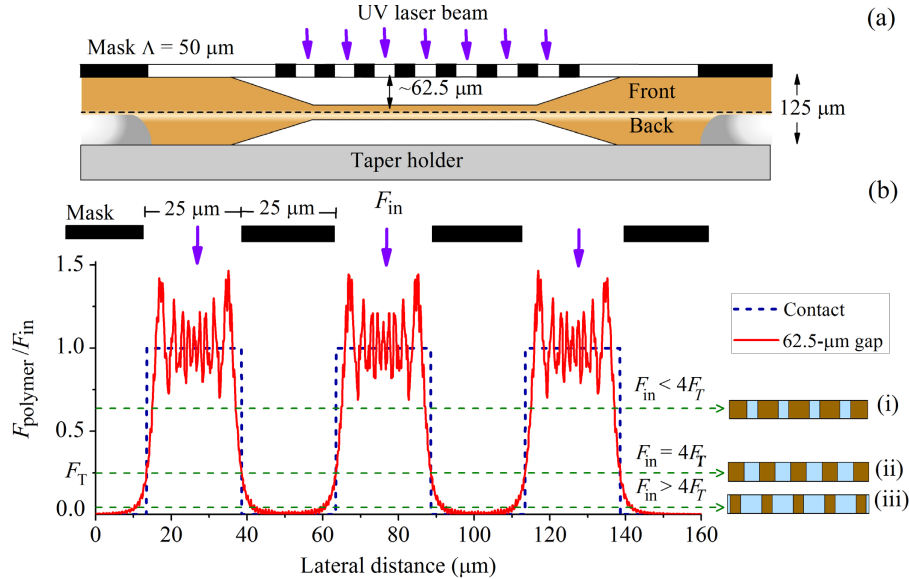


Fig. 5. (a) A Schematic diagram of an ablation mask over a nonlinear taper. The mean gap between the mask and the taper waist is $\sim 62.5 \mu\text{m}$. (b) Simulated UV beam fluence (normalized with respect to incident fluence) on the nonlinear polymer coating. Case 1: the mask is in direct contact with the polymer coating (dashed blue line); Case 2: a $62.5 \mu\text{m}$ gap exists between the mask and the polymer coating (red line). The three dashed green horizontal lines indicate the ablation threshold (F_T) for three different incident fluences F_{in} given in the text. Their corresponding ablated polymer coating patterns are individually labelled as (i), (ii), and (iii).

We model the UV beam diffraction using the standard approach [32]. As shown in Fig. 5, we assume: 1) the incident beam is a uniform plane wave with wavelength 248 nm and fluence F_{in} ; 2) the gap distance between the mask and the polymer surface is $62.5 \mu\text{m}$; and 3) the ablation mask allows 100% transmission within the $25 \mu\text{m}$ slits and completely blocks UV light elsewhere. The calculated beam fluence on the polymer coating ($F_{polymer}$) is shown in Fig. 5(b). For direct contact (i.e., no gap), $F_{polymer}$ is exactly a square wave form (dashed blue line). And as long as the laser intensity is above the ablation threshold, the mask pattern is exactly transferred onto the polymer coating. However, if a small gap (e.g., $62.5 \mu\text{m}$) exists, $F_{polymer}$ exhibits multiple diffraction fringes (red line).

Fortunately, we can take advantage of the threshold characteristic of laser ablation to eliminate these undesired diffraction fringes. In the following calculations, we assume that polymers in regions where $F_{polymer} > F_T$ are completely removed, and remain intact if otherwise. Then, at $F_{in} \sim 4F_T$, even within the diffraction fringes, the UV beam fluence $F_{polymer}$ is higher than the ablation threshold F_T , which corresponds to the middle dashed horizontal line with label (ii), over the entire open region of the mask. Under the above assumptions, the mask pattern is almost exactly transferred onto the polymer coating without any fringes, as seen in figure inset (ii). For the case with lower UV fluence ($F_{in} = 1.6F_T$), the ablation threshold F_T is now represented by the upper dashed horizontal line (i). In this case, the polymer coating is “under-exposed” and the ablated section length becomes shorter, as seen

in inset (i). For a higher incident fluence, ($F_{in} = 10F_T$), the ablation threshold and the polymer coating image are represented as the bottom horizontal dashed line and inset (iii), respectively. Due to “over-exposure”, the length of the ablated sections becomes longer. In accordance with the results in Fig. 4(b), we use the fluence of 160 mJ/cm^2 (which is four times of PAH/PB threshold, 40 mJ/cm^2) for the ablation-based patterning of PAH/PB film on a taper.

3.2 Visualization and characterization

After ablation, the first step in characterizing the ablated periodic polymer coating is direct visualization. Since the thickness of the self-assembled PAH/PB film is only $\sim 0.5 \text{ nm/bilayer}$ [10], the polymer coating must be quite thick to generate sufficient contrast for optical imaging. Figure 6(a) shows two phase contrast microscope images of a fiber taper coated with 150-bilayer PAH/PB film. The images clearly reveal the periodic polymer pattern defined by the ablation process. To further enhance the contrast of optical microscopy, we intentionally incorporated a small amount of Texas Red (TR) (emission peak around 620 nm) onto the polymer coating. The advantage of TR is that the dye is negatively charged and highly soluble in water. Therefore, it can be directly mixed into the solution of positively-charged PAH molecules and form monolayers of PAH-TR (where a small fraction of PAH monomers are bound to the TR dye) during deposition [33]. High-contrast images of a patterned 20-bilayer (PAH-TR)/PB film, rendered using a confocal fluorescence microscope (Zeiss LSM 510 NLO + VIS), are shown in Fig. 6(b). Periodic patterns can be clearly observed on both the front and the back sides of the taper, even at large taper radius. Additionally, we do not observe any changes in ablation patterns along the azimuthal direction. This result suggests that the ablation laser pulses can propagate through the fiber structure with relatively low attenuation, which is consistent with the relatively high UV transmission in fused silica at the laser wavelength. The images in Fig. 6 confirm the feasibility of using this laser ablation technique to produce a periodic nonlinear structure on a taper structure for QPM.

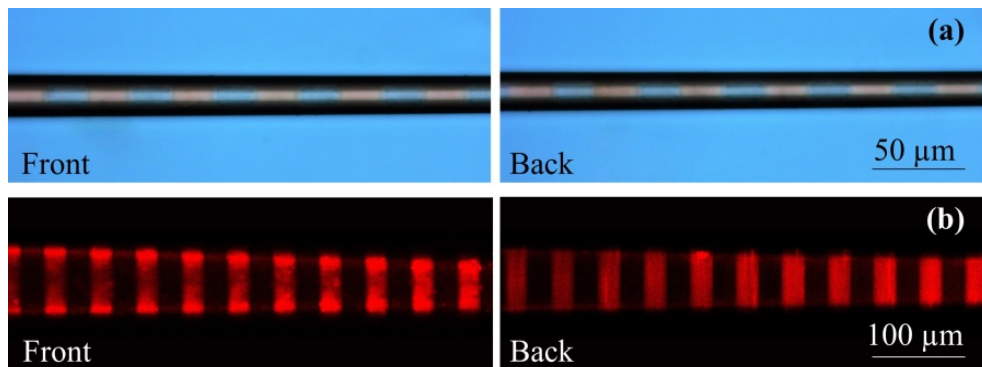


Fig. 6. (a) Images of a fiber taper with periodic coatings of 150-bilayer PAH/PB film. (b) Confocal fluorescence microscope images of a periodic pattern of the 20-bilayer (PAH-TR)/PB film. Both imaging techniques confirm that well-defined periodic patterns can be produced at the front and the back of the taper.

To ensure that the ablation process does not damage the nonlinear taper and incur excessive loss, we monitor the transmission loss of the nonlinear taper during its fabrication. The incident signal is provided by a fiber-connected white light source (DH-2000, Ocean Optics). The power spectra of transmitted signals are measured using a spectrometer (HR4000, Ocean Optics). We directly splice the taper into a fiber cable that connects the white light source with the spectrometer. The taper transmission loss spectrum is obtained by comparing the spectra of the transmitted optical signal measured with and without the taper sample. Figure 7 shows taper loss spectra measured at different fabrication steps. The black

line is obtained using a bare taper. After uniformly coating this bare taper with 10-bilayer PAH/PB film, taper loss is again measured and shown as the red line. Due to absorption by the PAH/PB coating [13], the overall taper transmission loss increases. Next, we fabricate the periodic nonlinear coating by partially removing the PAH/PB film using laser ablation, and again measure its loss spectrum. The taper transmission loss (blue line) actually decreases. The reduction in taper loss can be explained by the lower material absorption, since approximately half of the PAH/PB coating is removed. Overall, our results suggest that the ablation process does not induce significant loss in the wavelength range of interest.

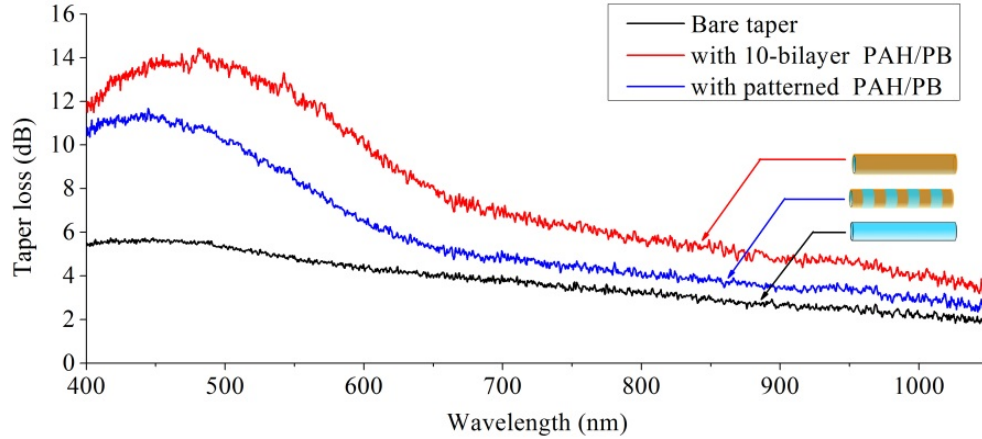


Fig. 7. Loss spectra of a fiber taper with different coating structure: (black line) bare taper, (red line) the taper after coating with 10-bilayer PAH/PB film, and (blue line) after patterning by laser ablation.

4. SHG measurements of the periodically patterned nonlinear taper

The SHG measurement system is shown in Fig. 8(a). We use an OPO (Opolette 355, OPOtek) to generate linearly polarized pump pulses in the range of 1100-1300 nm, with 10 ns pulse width and 20 Hz repetition rate. Two long-pass filters (F1 and F2) are incorporated to block all short-wavelength noise. A polarizer (P) is used to control pump power. The pump light is coupled into a multimode fiber (50 μm core, 125 μm cladding, NA = 0.22) through a 40X objective lens (OL1) while the output light is collected and collimated back into free space by another similar objective lens (OL2). Due to the noncircular beam profile produced by the OPO, the coupling efficiency for the pump light is typically between 10% - 15%. For different taper measurements, we directly splice any given taper sample within the multimode fiber, thus avoiding any modification to the free space optical system. The output beam is filtered by a short-pass filter (F3) to eliminate the pump light, allowing only the SHG signal to pass through. The second harmonic wavelength is further verified by a monochromator (Connerstone 74111, Newport) before detection by a photomultiplier tube (PMT). Here the transmission wavelength of the monochromator is automatically set at half of the OPO pump wavelength by computer. The SHG power from the PMT is then measured using an oscilloscope and acquired by a computer.

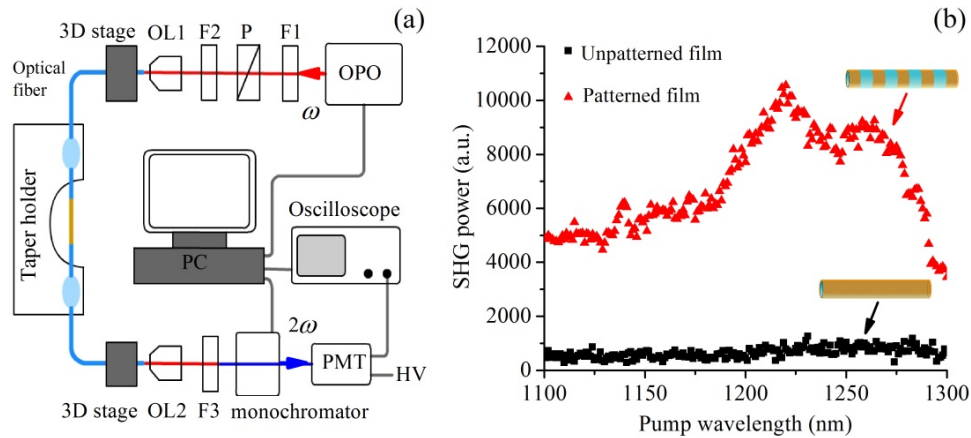


Fig. 8. (a) Schematic diagram of the experimental setup to measure SHG power generated by a patterned nonlinear fiber taper. (b) The measured SHG intensity at different pump wavelength for (square ■) a taper with uniform coating of 10-bilayer PAH/PB, and (triangles ▲) the same sample with ablation patterning.

Figure 8(b) shows the SHG intensity measured using a nonlinear fiber taper with waist radius of $3.75 \mu\text{m}$. The radial profile and transmission loss of the same taper have been shown in Fig. 4 and Fig. 7, respectively. During the pump wavelength scan, the peak pump power at the fiber output (i.e., after taper transmission) is fixed at $P_{\omega} = 200 \text{ W}$ for all measurements. Due to the low pump power and the relatively large taper diameter, the SHG signal produced by the bare taper alone is undetectable. Next, we uniformly coat this bare taper with 10-bilayer PAH/PB film, and measure its SHG intensity. Finally, we use laser ablation to produce periodically patterned nonlinear coating on the same fiber, with spatial pitch $\Lambda = 50 \mu\text{m}$, and again measure its SHG intensity under identical experimental conditions. The spectral responses are shown in Fig. 8(b). As can be seen from the figure, the output SHG signal generated from the taper with uniform coating (black squares) is quite low and does not possess any notable spectral features such as large dips or peaks. These observations are consistent with the non-phase-matched nature of the uniformly coated nonlinear taper. For the taper with spatially periodic coating, on the other hand, we observe a much stronger SHG intensity (red triangles) with clear spectral features. Quantitatively, at the spectral peak (pump wavelength $\sim 1220 \text{ nm}$), the SHG intensity produced by the patterned nonlinear taper is ~ 15 times stronger than the SHG intensity of the uniformly coated taper. This experimental result is clearly consistent with our expectation that a nonlinear taper with QPM should enhance SHG efficiency.

5. Analysis and discussion

5.1 Theoretical analysis of QPM in the nonlinear taper

Our previous work [11,12] has shown that in a cylindrical fiber covered with radially aligned nonlinear molecules, the SHG process must satisfy certain selection rules. If the pump beam takes the form of the HE_{11} mode ($l = 1$), the mode associated with the second harmonic signal must satisfy either $l = 0$ or 2 , which means the likely candidates for the second harmonic mode are the TM_{01} , TE_{01} , and HE_{21} mode. Since the $\chi^{(2)}$ tensor is dominated by the rrr component, the second harmonic mode must possess a strong radial component, which eliminates the TE_{01} mode from consideration. Our discussion, therefore, focuses on the TM_{01} and the HE_{21} mode. Using β_{ω} and $\beta_{2\omega}$ to denote the propagation constant of the pump and the second harmonic mode, we define the coherence length (L_{coh}) as:

$$L_{\text{coh}} = \frac{\pi}{\Delta\beta}, \quad (2)$$

where $\Delta\beta = 2\beta_{\omega} - \beta_{2\omega}$. Once L_{coh} is determined, the spatial periodicity (Λ) of the $\chi^{(2)}$ grating required for QPM is simply $\Lambda = 2L_{\text{coh}}$. In Fig. 9(a), we numerically calculate the value of L_{coh} for different fiber taper radius a and second harmonic mode. The pump wavelength is restricted to 1100 – 1300 nm, in accordance with our experiments. We assume the fiber cladding is air and the core is pure silica, where the wavelength dependence of the silica refractive index n is given in [34]. Based on the aforementioned requirement ($\Lambda = 2L_{\text{coh}}$) and the results in Fig. 9(a), we observe that the 50 μm nonlinear grating pitch Λ is suitable for QPM in typical taper radius ranging from 3.0 to 5.0 μm .

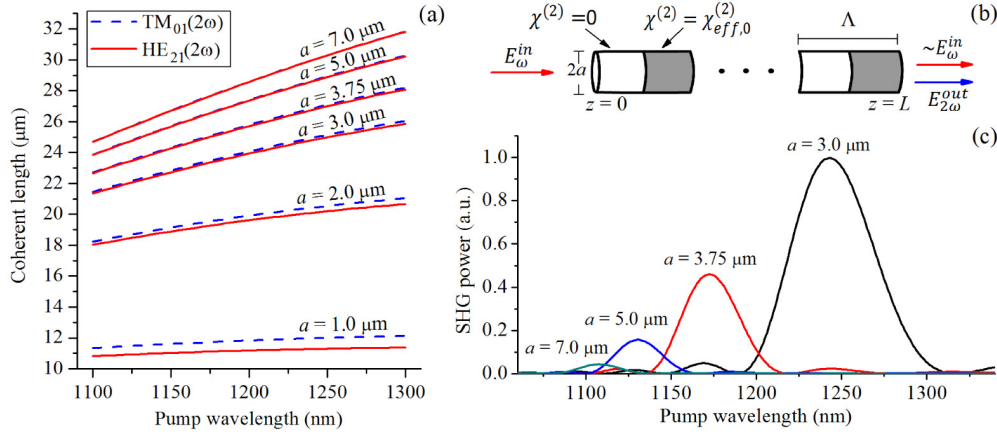


Fig. 9. (a) Numerical result for the coherence length, L_{coh} , of SHG in a nonlinear fiber taper with pump wavelength between 1100 and 1300 nm, and for different taper radius. (b) Schematic illustration of the modulation of the effective $\chi^{(2)}$ along the direction for light propagation, and the configuration for SHG analyzed in section 5. (c) The SHG power versus pump wavelength for different taper radius, obtained using Eq. (6). The results are normalized such that the highest SHG power is set to 1.

For a more quantitative estimate of SHG produced by the nonlinear taper, we follow [11,13] and approximate the polymer-coated section as a homogenous material with an effective nonlinearity $\chi_{\text{eff},0}^{(2)} \approx (\delta/a)\chi_{\text{rrr}}^{(2)}$, where δ and $\chi_{\text{rrr}}^{(2)}$ represent the thickness and the nonlinear susceptibility of the polymer coating. This approximation allows us to reduce the original three-dimensional problem into a one-dimensional (1D) one, as illustrated in Fig. 9(b). Assuming no pump depletion, the second harmonic field $E_{2\omega}$ in the 1D equivalent structure satisfies [11,13]:

$$\frac{dE_{2\omega}}{dz} = -i \frac{\omega}{\sqrt{\pi\epsilon_0}v_g n^3} |E_{\omega}^{\text{in}}|^2 \chi_{\text{eff}}^{(2)}(z) e^{-i\Delta\beta z}, \quad (3)$$

where E_{ω}^{in} is the incident pump field amplitude, v_g is the group velocity of the second-harmonic light, $\chi_{\text{eff}}^{(2)}(z)$ represents the spatially-dependent effective second-order nonlinear susceptibility, and can be expressed in terms of a Fourier series:

$$\chi_{\text{eff}}^{(2)}(z) = \chi_{\text{eff},0}^{(2)} \sum_m G_m e^{ik_m z}, \quad (4)$$

where the wavevector of the m^{th} Fourier component is $k_m = 2\pi m / \Lambda$, and $G_m = (1/2)e^{im\pi/2} \text{sinc}(m\pi/2)$. By integrating Eq. (3) along the z direction, assuming no incident second harmonic field and applying Eq. (4), we can express the field amplitude of the second harmonic signal $E_{2\omega}^{\text{out}}$ at the output ($z = L$) as,

$$E_{2\omega}^{\text{out}} = -i \frac{\omega}{\sqrt{\pi} \epsilon_0 V_g n^3} |E_{\omega}^{\text{in}}|^2 L \chi_{\text{eff},0}^{(2)} \left[\sum_m G_m e^{-i\Delta\beta_m L/2} \frac{\sin(\Delta\beta_m L/2)}{(\Delta\beta_m L/2)} \right], \quad (5)$$

where $\Delta\beta_m = \Delta\beta - k_m = \Delta\beta - 2\pi m / \Lambda$. To accurately evaluate $E_{2\omega}^{\text{out}}$, we typically include multiple Fourier components with $|m| \leq 5$.

In our experiments, we set the pump peak power P_{ω} at 200 W and measure SHG power $P_{2\omega}$ as a function of pump wavelength. To theoretically analyze this scenario, we note that $P_{2\omega}$ can be approximated as $P_{2\omega} = (1/2)\epsilon A_{\text{eff},2\omega} V_{g,2\omega} |E_{2\omega}^{\text{out}}|^2$, where $A_{\text{eff},2\omega}$ is the effective mode area for the SHG mode. A similar relation also holds for the pump beam, except all parameters should be evaluated at the pump frequency ω . For the wavelength range of interest, we further assume: 1) A_{eff} can be approximated as πa^2 and 2) the group velocity for both the pump and the second harmonic signal is c/n . With these considerations, we can recast Eq. (5) in terms of pump and SHG power, which leads to:

$$P_{2\omega} \approx \left\{ \frac{2\delta^2 |\chi_{rrr}^{(2)}|^2}{\epsilon_0^3 c^3 \pi^2 n^5} \right\} P_{\omega}^2 \omega^2 \frac{L^2}{a^4} \left| \sum_m G_m e^{-i\Delta\beta_m L/2} \frac{\sin(\Delta\beta_m L/2)}{(\Delta\beta_m L/2)} \right|^2. \quad (6)$$

Note that in Eq. (6), the fraction in the curly bracket $\{\}$ can be regarded as a constant that does not depend on experimental parameters such as pump frequency and taper radius. Since the pump peak power is fixed in our experiments, we can essentially treat the curly bracket term and P_{ω} as a single normalization constant. The rest of the terms in Eq. (6) are more interesting, and reveal the dependence of SHG power on taper radius, pump wavelength, and interaction length L . In Fig. 9(c), we choose the normalization constant to be the same for all taper samples, and use Eq. (6) to estimate the spectral dependence of $P_{2\omega}$ for different taper radius. We assume $\Lambda = 50 \mu\text{m}$, $L = 1 \text{ mm}$ and the SHG mode is TM_{01} . The most noteworthy feature of Fig. 9(c) is that as the taper radius increases from 3 to 7 microns, the SHG intensity peak for pump wavelength slowly blue-shifts from 1250 nm to 1100 nm. Similar results are found if we assume the SHG mode to be the HE_{21} mode.

Our experimental results in Fig. 8(b) show that for a nonlinear taper with $3.75 \mu\text{m}$ waist radius, there is an SHG peak for pump wavelength in the vicinity of 1220 nm. This result is in reasonable agreement with our theoretical estimate in Fig. 9(c) which suggests that a periodically patterned taper with uniform taper radius in the range of 3-3.5 μm should exhibit an SHG peak for pump wavelength in the range of 1200 – 1250 nm. Given the fact that the results in Fig. 9(c) are obtained without any fitting parameter, the agreement between theory and experiment is reasonable. Additionally, we notice that the experimentally measured second harmonic signal remains reasonably strong within a broad pump wavelength range. Such a “spectral broadening” can perhaps be explained by the non-uniform taper profile.

It is worthwhile to compare the nonlinear taper investigated here with other types of nonlinear materials. In Ref [10], it has been shown that the $\chi^{(2)}$ coefficient of PAH/PB film is dominated by the zzz component, with $\chi_{zzz}^{(2)} = 21 \text{ pm/V}$. This $\chi^{(2)}$ coefficient is about one third of LiNbO_3 and is considerably larger than that of poled fibers (typically a fraction of 1 pm/V [35]). As discussed earlier, the effective $\chi^{(2)}$ of a nonlinear taper with taper radius a and

nonlinear coating thickness δ can be estimated as $\chi_{\text{eff}}^{(2)} \approx (\delta/a)\chi_{\text{zzz}}^{(2)}$. For instance, with $a = 1 \mu\text{m}$ and $\delta = 30 \text{ nm}$, its effective $\chi^{(2)}$ is approximately 0.6 pm/V and comparable with that of a poled fiber. More importantly, the second-order nonlinearity of the PAH/PB film originates from self-alignment of the PAH and PB molecules driven by strong intermolecular forces, and is therefore thermally stable, as shown in [10]. According to Eq. (6), the SHG efficiency can be significantly improved by using a highly uniform taper structure. Again, assuming $a = 1 \mu\text{m}$ and $\delta = 30 \text{ nm}$, for a periodically patterned nonlinear taper with spatial pitch $\Lambda = 24 \mu\text{m}$ and total length $L = 5 \text{ mm}$, the SHG efficiency of the nonlinear taper is 12% under 400 W pump peak power, as shown in Fig. 10(a). (The spatial pitch for $\chi^{(2)}$ is changed to $24 \mu\text{m}$ for the thinner taper. This value satisfies QPM between the fundamental mode and the TM_{01} mode, as can be seen from Fig. 9(a).) Despite the high SHG efficiency, the SHG bandwidth remains reasonable. As shown in Fig. 10(a), for the aforementioned taper structure, the full width half maximum for SHG peak is $\sim 25 \text{ nm}$.

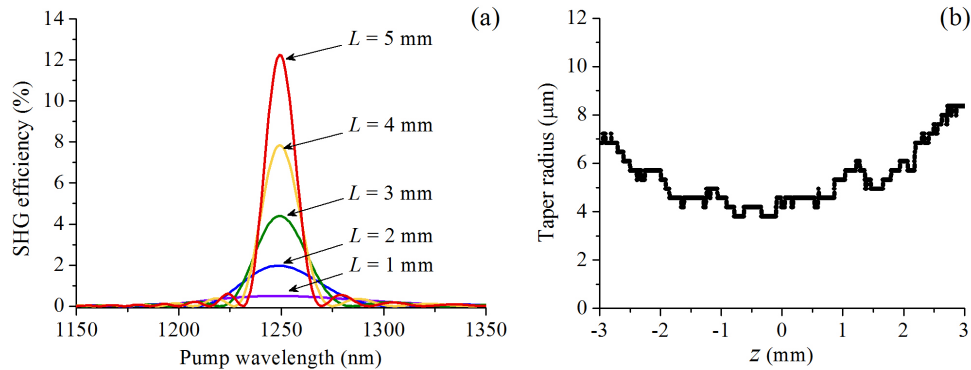


Fig. 10. (a) Theoretical estimate of SHG conversion efficiency from a taper with uniform radius of $a = 1 \mu\text{m}$, nonlinear film thickness $\delta = 30 \text{ nm}$, grating period $\Lambda = 24 \mu\text{m}$, and excited by pump power $P_o = 400 \text{ W}$. L denotes total taper length. (b) The profile of taper radius near its waist. This result is a magnified view of the taper radius profile shown in Fig. 4(b).

In practice, fiber taper is perhaps not the ideal platform for realizing highly uniform QPM. Figure 10(b) provides a magnified view of the taper waist radius shown in Fig. 4(b). Despite fluctuations in the extracted taper radius value, which might be due to the resolution limit of the microscopy system, it is clear that the taper radius is far from uniform even in the waist region. According to Fig. 9(a), the coherent length for QPM changes rapidly as the taper radius changes. Therefore, the non-uniform taper profile might account for the relatively low peak enhancement (~ 15) as well as the broad spectral range for SHG shown in Fig. 8(b). Additionally, it may also be possible that within the taper waist, the pump field is not purely in the fundamental HE_{11} mode. To resolve these problems, we are currently considering alternative fiber structures such as side-polished fibers [36] and D-shaped fibers [37]. Furthermore, photonic crystal fibers (PCF) may also be suitable for demonstrating quasi-phase-matched second order nonlinearity. A few interesting examples of PCF that are compatible with the requirements for nonlinear coating can be found in [38]

5.2 Spatially selective patterning of other nanomaterials

Besides second-order nonlinearity, the ablation technique can also be used to pattern silica structures with other types of functional nanomaterials. As a proof of concept demonstration, we deposit a layer of Au NPs onto the taper surface in a spatially selective manner. The result is also used to validate the “exposure” analysis summarized in Fig. 5(b).

To create a periodic pattern of Au NPs, we utilize the laser ablation process to generate a periodic surface charge pattern across the taper surface. Specifically, we “cap” the nonlinear film coating with a positively-charged PAH layer. After laser ablation using the same mask,

the regions with exposed silica surface become negatively charged [39]. Then, we immerse the patterned taper structure in a colloidal solution of negatively charged Au NPs (30 nm, Ted Pella Inc.) for 1 hour. The Au NPs are preferably adsorbed onto the surface of the nonlinear film via strong electrostatic interaction. In comparison, the bare silica surface (exposed by UV ablation) tends to repel Au NPs, since both are negatively charged.

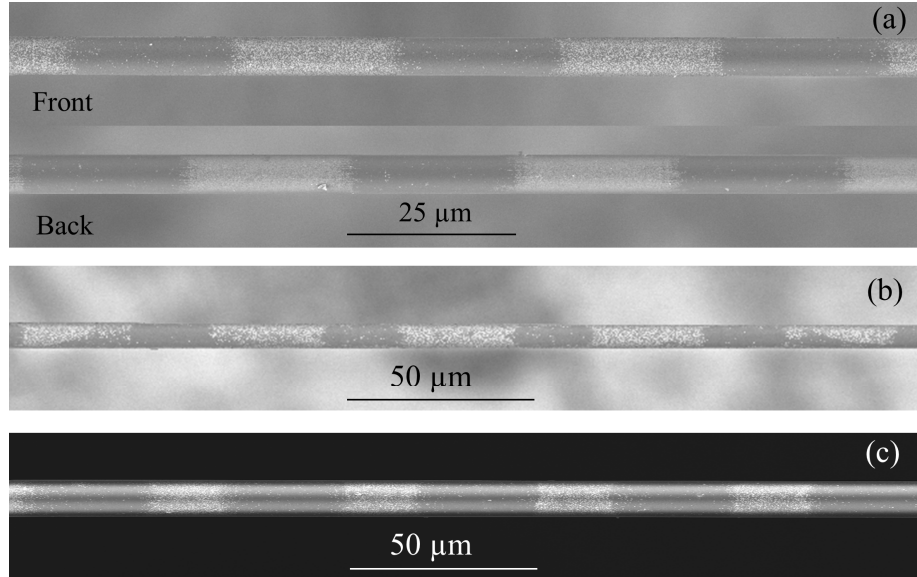


Fig. 11. (a) SEM images showing a periodic pattern of Au NPs near a taper waist, produced by ablation patterning with $F = 4F_T$. (b) and (c) show spatial patterns of Au NPs on similar tapers, where laser ablation of the polymer coating is performed with laser fluence $F < 4F_T$ and $F > 4F_T$, respectively.

Figure 11 shows several SEM images of periodic patterns of 10-bilayer PAH/PB films covered with Au NPs. The ablated areas can be clearly identified as the darker segments with relatively few attached NPs, whereas sections covered by the polymer appear lighter due to the large Au NP density. All three samples are fabricated using the same setup in Fig. 5(a) and the same mask. However, by adjusting the UV laser fluence, we can generate different NP attachment patterns. For example, with $F = 160 \text{ mJ/cm}^2$ ($F \sim 4F_T$), as predicted by pattern (ii) in Fig. 5, the NP pattern on the fiber taper is almost the same as the mask pattern. Furthermore, the front and the back of the taper possess similar NP patterns, which suggest that UV beam absorption / diffraction by the fiber taper is not a significant factor in UV ablation. Figure 11(b) shows an under-exposed case, i.e., pattern (i) in Fig. 5, where a lower fluence of $F = 65 \text{ mJ/cm}^2$ ($F < 4F_T$) is used. Clearly, the ablated segments become shorter. On the opposite end, by using a higher UV fluence 400 mJ/cm^2 ($F > 4F_T$), the taper is over-exposed and the ablated segments become longer (Fig. 11(c)), in accordance with pattern (iii) in Fig. 5.

6. Conclusion

We experimentally demonstrate the feasibility of using a UV laser beam to pattern a second-order nonlinear self-assembled organic film and achieve QPM in silica-based nonlinear fiber tapers. Through planar sample characterizations, we identify the fluence threshold for laser ablation and confirm the empirical relationship that links the amount of material removal and beam parameters such as pulse fluence and the number of pulses. Using UV ablation, we produce a spatially periodic second-order nonlinearity on the taper surface that can satisfy the QPM condition for SHG. We find that the second harmonic signal produced by the patterned

nonlinear taper is enhanced by a factor of 15 in comparison with the same taper with a uniform nonlinear coating. The spectral peak of the measured second harmonic signal is also largely consistent with theoretical predictions. This UV ablation technique can also be used to pattern other types of functional nanomaterials on silica microstructures with curved surfaces.

Acknowledgments

We gratefully acknowledge support by the National Science Foundation (EFRI-1433311), and the VT-MENA program.